

Fig. 4. Nondegenerate ($\Omega_1 \neq \Omega_2$) spectral mapping of a single eigenstate. Each spectrum represents a different spectral position of the pump (Ω_1), which is indicated by the arrow.

$$f_n(\Omega_1, \Omega_2) = \frac{1}{8(\gamma_n + i\Delta_{n_1})} \left[\frac{1}{\Gamma_n} \left(\frac{1}{\gamma_n - i\Delta_{n_1}} + \frac{1}{\gamma_n + i\Delta_{n_1}} \right) + \frac{1}{\Gamma_n + i(\Delta_{n_2} - \Delta_{n_1})} \left(\frac{1}{\gamma_n - i\Delta_{n_1}} + \frac{1}{\gamma_n + i\Delta_{n_1}} \right) \right] + c.c. \quad (3)$$

where $\Delta_{n_i} = \omega_n - \Omega_i$ and indices 1 and 2 refer to the pump and probe fields, respectively (29). As discussed in (13), the line shape is distinctive in two limits. In the limit where excitation decoherence rate ($T_2^{-1} = \gamma_n$) greatly exceeds the energy relaxation rate ($T_2^{-1} = \Gamma_n$), the line shape is characterized by a simple Lorentzian resembling a spectral hole with width $2\hbar T_1^{-1}$ centered at the pump frequency superimposed on a much broader Lorentzian with width $2\hbar T_2^{-1}$ centered at the quantum dot exciton resonance. In the limit where the only decoherence is due to energy relaxation (i.e., $T_2^{-1} \approx T_1^{-1}/2$), the line shape transforms markedly to one that arises from interference, resembling dispersion, distinctly differentiating the two limits. The data in Fig. 4 show this interference line shape unambiguously; as the pump field is tuned away from line center, a dispersion-like line shape due to the coherent contribution emerges in the nonlinear response. This is consistent with no substantial pure dephasing, such that $T_2 \approx 25$ ps and $T_1 \approx 1/\Gamma_n \approx 16 \pm 3$ ps. This lack of extra dephasing allows for the coherent coupling of the optical fields through the eigenstate and the temporal modulation of the excitation of a single exciton [population pulsations (30)] at the difference

frequency $\Omega_2 - \Omega_1$ (up to ~ 12 GHz for the eigenstate examined in Fig. 4). The single resonance dephasing rate discussed above is consistent with the ensemble-averaged dephasing rate extracted from Fig. 1B and similar to that reported in (13).

Moving beyond the paradigm of single exciton spectroscopy, the optical LDOS has been obtained for a quantum dot system. At the single eigenstate level, our two optical fields are coherently coupled through the excitonic resonance, allowing us to determine the various time scales associated with the excitation. These experiments have laid the foundation for selectively addressing and controlling individual eigenstates in a coherent manner through spatial as well as spectral discrimination. This technique is applicable to any optically active system in the vicinity of the sample surface, such as other semiconductor nanostructures or single molecules, making it easily adaptable to the changing frontier of nano-optics and quantum-information technology.

References and Notes

- D. Gammon, E. S. Snow, B. V. Shanabrook, D. S. Katzer, D. Park, *Phys. Rev. Lett.* **76**, 3005 (1996).
- S. Fafard, R. Leon, D. Leonard, J. L. Merz, P. M. Petroff, *Phys. Rev. B* **50**, 8086 (1994).
- H. Hess, E. Betzig, T. D. Harris, L. N. Pfeiffer, K. W. West, *Science* **264**, 1740 (1994).
- A. Imamoglu et al., *Phys. Rev. Lett.* **83**, 4204 (1999).
- M. F. Crommie, C. P. Lutz, D. M. Eigler, *Nature* **363**, 524 (1993).
- J. Levy et al., *Phys. Rev. Lett.* **76**, 1948 (1996).
- M. Vollmer et al., *Appl. Phys. Lett.* **74**, 1791 (1999).
- O. Mauritz, G. Goldoni, F. Rossi, E. Molinari, *Phys. Rev. Lett.* **82**, 847 (1999).
- S. Savasta, G. Martino, R. Giralda, *Phys. Rev. B* **61**, 13852 (2000).
- B. Hanewinkel, A. Knorr, P. Thomas, S. W. Koch, *Phys. Rev. B* **55**, 13715 (1997).
- G. W. Bryant, *Appl. Phys. Lett.* **72**, 768 (1998).
- J. Barenz, O. Hollricher, O. Marti, *Rev. Sci. Instrum.* **67**, 1912 (1995).
- N. H. Bonadeo et al., *Phys. Rev. Lett.* **81**, 2759 (1998).
- G. Chen et al., *Science* **289**, 1906 (2000).
- Q. Wu, R. D. Grober, D. Gammon, D. S. Katzer, *Phys. Rev. Lett.* **83**, 2652 (1999).
- E. Yablonovich, T. Gmitter, J. P. Harbison, R. Bhat, *Appl. Phys. Lett.* **51**, 2222 (1987).
- M. K. Lewis, P. Wolanin, A. Gafni, D. G. Steel, *Opt. Lett.* **23**, 1111 (1998).
- G. Chen et al., unpublished data.
- J. T. Remillard et al., *Phys. Rev. Lett.* **62**, 2861 (1989).
- H. Wang, M. Jiang, D. G. Steel, *Phys. Rev. Lett.* **65**, 1255 (1990).
- The simple theoretical treatment of the nano-optical response described herein is adequate only in the limit that the spatial resolution comfortably exceeds the length scale that characterizes Coulomb correlations, i.e., the excitonic Bohr radius. Below this limit, a new regime is entered in which the nonlocal character of the light-matter interaction and Coulomb correlation effects dominate the local optical response; a nonlocal formulation must then be used [see (8, 9)].
- U. Jahn et al., *Phys. Rev. B* **56**, R4387 (1997).
- J. Erland et al., *Phys. Rev. B* **60**, R8497 (1999).
- T. Takagahara, *Phys. Rev. B* **39**, 10206 (1989).
- E. Runge, R. Zimmermann, *Phys. Stat. Sol. b* **206**, 167 (1998).
- F. Intonti et al., *Phys. Rev. Lett.* **87**, 076801 (2001).
- J. R. Guest et al., paper presented at Nonlinear Near-Field Spectroscopy and Microscopy of Single Excitons in a Disordered Quantum Well, QELS, 2000.
- J. R. Guest et al., data not shown.
- In our geometry, each field serves as both the pump and probe.
- P. Meystre, M. Sargent, *Elements of Quantum Optics* (Springer-Verlag, New York, ed. 2, 1991).
- This work was supported in part by the Office of Naval Research, the National Security Agency, and Advanced Research and Development Activity under Army Research Office contract number DAAG55-98-1-0373, the Air Force Office of Scientific Research under grant number F49620-99-1-0045, the NSF under grant DMR 0099572, and DARPA/Spins. One of the investigators (D.G.S.) thanks the Guggenheim Foundation for their support.

22 June 2001; accepted 15 August 2001

Hydrogen Sensors and Switches from Electrodeposited Palladium Mesowire Arrays

Frédéric Favier,¹ Erich C. Walter,² Michael P. Zach,² Thorsten Benter,² Reginald M. Penner^{2*}

Hydrogen sensors and hydrogen-activated switches were fabricated from arrays of mesoscopic palladium wires. These palladium "mesowire" arrays were prepared by electrodeposition onto graphite surfaces and were transferred onto a cyanoacrylate film. Exposure to hydrogen gas caused a rapid (less than 75 milliseconds) reversible decrease in the resistance of the array that correlated with the hydrogen concentration over a range from 2 to 10%. The sensor response appears to involve the closing of nanoscopic gaps or "break junctions" in wires caused by the dilation of palladium grains undergoing hydrogen absorption. Wire arrays in which all wires possessed nanoscopic gaps reverted to open circuits in the absence of hydrogen gas.

Chemical sensors based on nanowires usually operate through a change in resistance induced by the surface adsorption of analyte

molecules. Tao and co-workers (1) have demonstrated that the conductivity of gold nanowires changes upon exposure to mole-

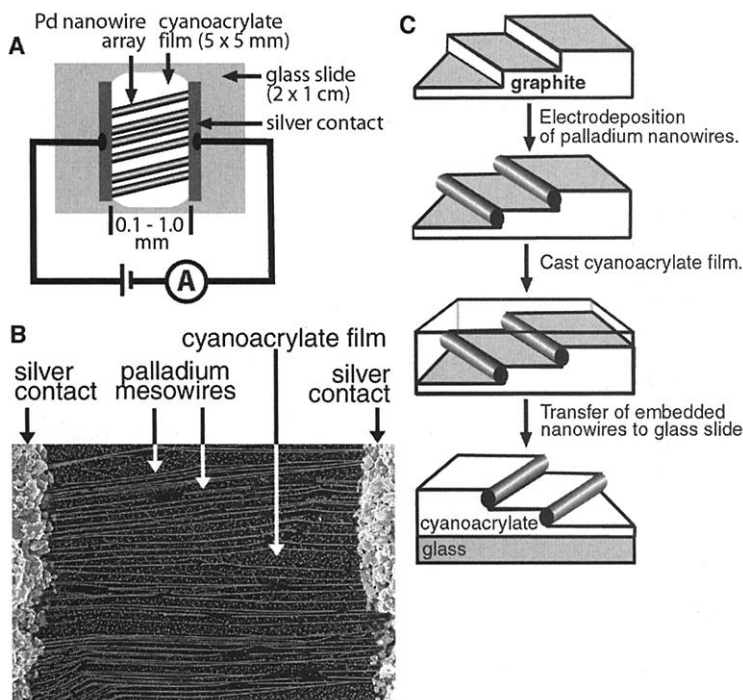


Fig. 1. (A) Schematic diagram of a PMA-based hydrogen sensor or switch. (B) SEM image [400 μm (h) by 600 μm (w)] of the active area of a PMA-based hydrogen sensor. (C) PMAs were prepared by electrochemical step edge decoration at graphite surfaces and transferred to a cyanoacrylate film.

cles capable of chemisorbing to gold surfaces such as thiols and amines. An analogous effect has been observed for single-walled carbon nanotubes that exhibit a resistance that changes upon exposure to gaseous oxygen (2), water (3), and amines (4).

We describe a wire-based sensor for the detection of hydrogen gas (H_2) that is based upon resistivity changes caused not by surface adsorption, but on changes in the structure of the wire itself. These sensors consist of up to 100 Pd mesoscopic (5) wires (henceforth, “mesowires”) arrayed in parallel (Fig. 1, A and B). Like conventional H_2 sensors based on macroscopic Pd resistors, the Pd mesowire array (PMA) in this sensor exhibits a resistance change upon exposure to H_2 . In contrast to all existing resistance-based H_2 sensors, however, the resistance of PMAs decreases instead of increasing in the presence of H_2 (6). We propose a new mechanism to account for this “inverse” response.

Palladium mesowires were electrodeposited from aqueous solutions of Pd^{2+} onto step edges present on a graphite surface, using a two-step procedure (Fig. 1C) (7). Starting with a freshly cleaved graphite surface, a 5-ms nucleation pulse of -0.2 V [versus sat-

urated calomel electrode (SCE)] was first applied. As shown in Fig. 2, this potential is well negative of the reversible potential for Pd deposition in these solutions ($+0.6$ to $+0.7$ V versus SCE). After this nucleation pulse, the growth of Pd mesowires was carried out using potentials in the ranges shown in gray in Fig. 2. These deposition potentials produced deposition current densities ranging from 30 to 60 $\mu\text{A cm}^{-2}$, and deposition times

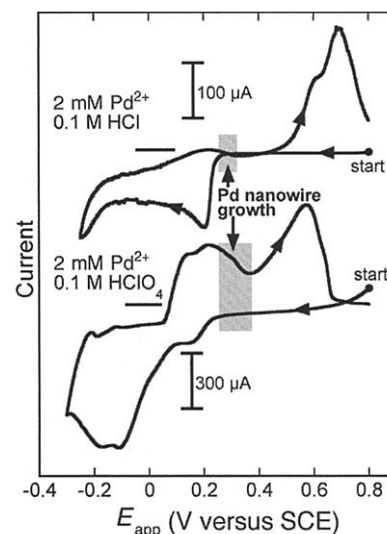


Fig. 2. Cyclic voltammograms for a graphite electrode in two aqueous Pd plating solutions, as indicated. The potential range used for the growth of Pd mesowires is indicated in gray.

for 200-nm-diameter mesowires were 10 min (8). Attempts to accelerate wire growth by using more negative potentials resulted in discontinuous structures.

The morphology of the Pd wires obtained by electrodeposition was dependent on the identity of the electrolyte present in the plating solution. Mesowires deposited from HCl solutions (Fig. 3, A and B) were rough and granular. The dimensions of the grains in these polycrystalline wires, as estimated from scanning electron microscope (SEM) images, ranged from 50 to 300 nm. The smallest continuous wires obtained from this solution were 150 nm in

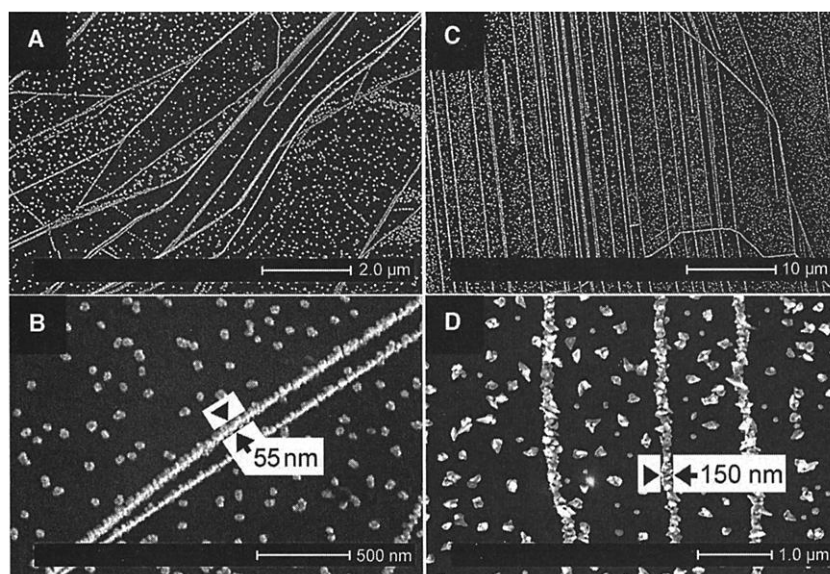


Fig. 3. (A and B) SEMs of Pd mesowires prepared by electrodeposition from aqueous 2.0 mM PdCl_2 and 0.1 M HCl. $E_{\text{dep}} = 0.3$ V, $t_{\text{dep}} = 900$ s. (C and D) SEMs of mesowires electrodeposited from aqueous 2.0 mM $\text{Pd}(\text{NO}_3)_2$ and 0.1 M HClO_4 . $E_{\text{dep}} = 0.3$ V, $t_{\text{dep}} = 150$ s.

¹UMR 5072 CNRS–Université Montpellier II, 34095 Montpellier, France. ²Department of Chemistry, University of California Irvine, Irvine, CA 92697–2025, USA.

*To whom correspondence should be addressed. E-mail: rmpenner@uci.edu

REPORTS

diameter. Deposition from HClO_4 solutions (Fig. 3, C and D) yielded wires with a smoother morphology. The grains in these wires were 10 to 50 nm in diameter. This smoother morphology permitted nanowires as narrow as 55 nm to be deposited. Both types of wires produced sharp electron diffraction patterns characteristic of face-centered cubic (fcc) Pd metal (8). Rough and smooth wires prepared using these two plating solutions behaved identically in the H_2 sensors and switches described below.

Freshly deposited Pd mesowires were transferred from the graphite electrode surface onto a glass slide coated with cyanoacrylate (Fig. 1C). When the cyanoacrylate film had hardened (8 hours), arrays of Pd mesowires were contacted with silver epoxy. A SEM image of the active area of a sensor (Fig. 1B) shows a PMA as horizontal lines contacted on each side by silver paint. In this device, the span between silver contacts was 300 to 500 μm . In other devices, this gap ranged from 100 μm to 1.0 mm. Only mesowires long enough to span these distances were involved in sensor function. The number of such mesowires, estimated from SEM images, varied from 20 to 100. The overall success rate for preparing H_2 sensors using this procedure was better than 50%.

PMAs were operated as H_2 sensors by applying a constant voltage of 5 mV between the silver contacts and measuring the current, which was between 1 and 20 μA . Two different modes of sensor operation were observed. "Mode I" sensors remained conductive in the absence of H_2 . The resistance of a mode I sensor decreased in the presence of H_2 (Fig. 4A), with the decrease related to the H_2 concentration. In nitrogen carrier gas at atmospheric pressure and room temperature, the limit of detection for a mode I sensor was 0.5% H_2 . The sensor exhibited a sigmoidal response curve (Fig. 4C) with a minimum resistance at 5 to 10% H_2 .

Mode II sensors were hydrogen-activated switches. In the absence of H_2 , the resistance of a mode II sensor became large (>10 megaohms; switch open). In this "wait state," the sensor dissipated no power and produced no noise. Typical data for a mode II sensor are shown in Fig. 4B. Above a threshold of approximately 2% H_2 , the switch closed and a device resistivity became measurable. Above this threshold H_2 concentration, the same sigmoidally shaped response curve seen for mode I sensors (Fig. 4C) was obtained.

Sensors were insensitive to a variety of gases other than H_2 , including Ar, He, N_2 , water vapor, and O_2 . The amplitude of the sensor response was unaffected by the presence of CO and CH_4 at concentrations up to 3%, but the response time to H_2 in the presence of CO was increased. The response of

sensors to D_2 was identical to that observed for H_2 .

A rise-time (baseline to 90% signal satu-

ration) of less than 80 ms has been observed for the response of mesowire-based sensors to 5% H_2 (Fig. 4D). This value is approxi-

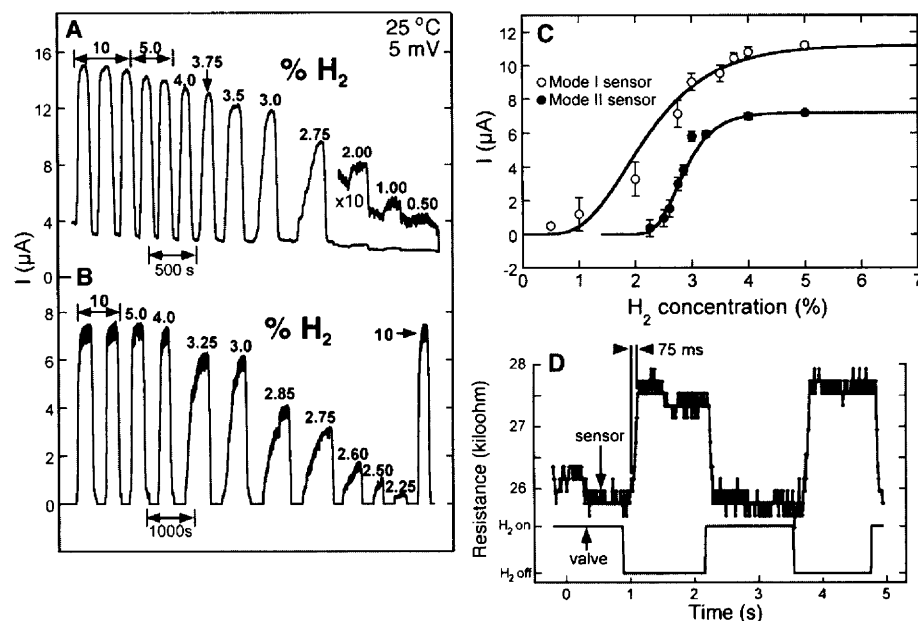


Fig. 4. (A) Current response of a mode I sensor to hydrogen/nitrogen mixtures (concentration of H_2 in percentage as shown). Data were acquired in random order of H_2 concentration. (B) Current response of a mode II sensor to hydrogen/nitrogen mixtures (concentration of H_2 in percentage as shown). Data were acquired in random order of H_2 concentration. (C) Current amplitude versus H_2 concentration for the two sensors of C (mode I) and D (mode II). (D) Sensor resistance versus time response for a mode I sensor. This is the only experiment of those shown in this figure for which the gas transport system was optimized for fast response. However, even in this case, it is likely that the switching time for valves was close to the apparent rise time of the sensor resistance (70 to 75 ms).

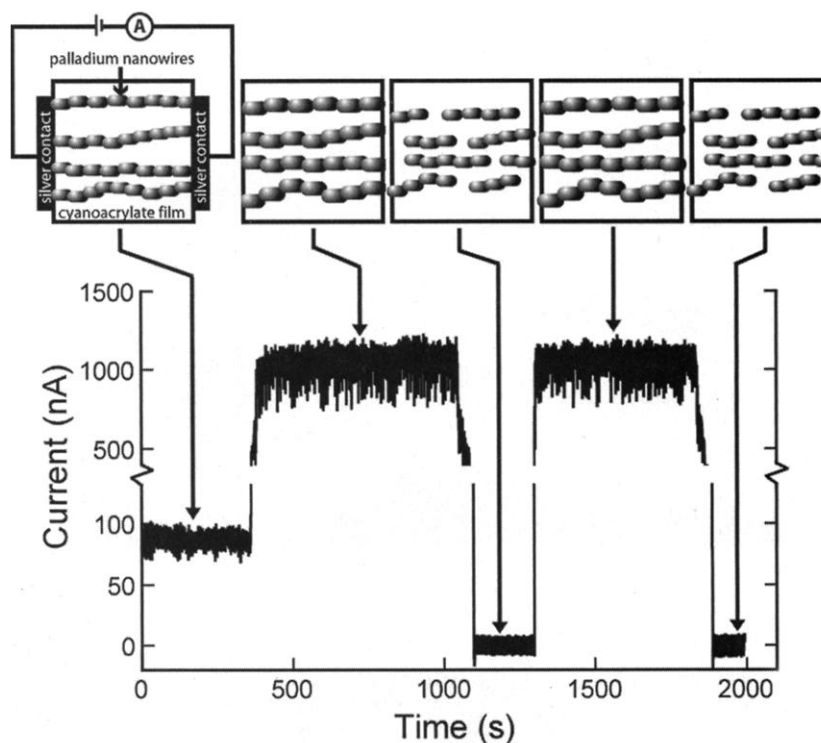


Fig. 5. The first exposure of a new sensor to hydrogen. In this case, an irreversible transition from mode I to mode II operation was observed (bottom). Shown at top is the mechanism proposed for mode II sensor operation. Mode I sensors operate by an identical mechanism, except that some mesowires remain conductive in the absence of hydrogen.

REPORTS

mately the response time of the gas flow system used for these measurements and represents an upper limit to the true response time of these sensors. If the true response time is dictated by the rate at which H_2 can diffusively saturate Pd grains in the mesowire, a faster response is expected. For 200-nm-diameter grains, for example, H_2 must diffuse $r = 100$ nm. The time, τ , required for this diffusional transport can be estimated from the diffusion coefficient for hydrogen in Pd, D , using $\tau = r^2/2D$. Assuming a mean value for D of 10^{-7} cm² s⁻¹ (9), $\tau = 0.5$ ms.

Macroscopic Pd resistors are commonly used as H_2 sensors, but in these devices, exposure to H_2 causes an increase in the resistance by a factor of up to 1.8 at 25°C (6). This resistance increase is caused by the increased resistivity of Pd hydride relative to pure Pd. A different mechanism must operate in the Pd mesowire-based devices described here.

The mechanism we propose is shown in Fig.

5. All of the PMAs we have investigated have been conductive before an initial exposure to H_2 (i.e., all devices were initially mode I). The first exposure to H_2 irreversibly modified the sensor: Either an increase in the baseline resistance (in air) of a sensor was observed for mode I devices or the resistance became large (the mode I device was converted into a mode II device). A resistance versus time transient for this conversion is shown in Fig. 5. After the first exposure to H_2 , exposure to air opens nanoscopic gaps in some (mode I) or all (mode II) mesowires in the sensor. These gaps open when the hydrogen-swollen Pd grains in each mesowire return to their equilibrium dimensions in the absence of hydrogen. Subsequently, it is the closing of these gaps or "break junctions" in the presence of H_2 that account for the decreased resistance of the sensor. Many or all of the mesowires in the array exhibit this switching behavior in mode I and mode II devices, respectively. This break junction mechanism provides an immediate explanation

for the device thresholds seen at 1 to 2% H_2 : At room temperature, the transition from α -phase to β -phase occurs at $P_{H_2} = 8$ torr in bulk Pd (6) which, at atmospheric pressure, corresponds to $\approx 1\%$ H_2 .

Acting in opposition to this "break junction" effect is an increase in resistance of each "closed" mesowire caused by the increased resistivity of Pd hydride. Mesowire-based sensors do not manifest this resistance effect in any observable way (e.g., sloping device current plateaus or baselines). This difference suggests that the change in mesowire resistance occurs on a time scale equal to, or faster than, the time required for the closing and opening of break junctions in these wires. As indicated earlier, this expectation is reasonable based on the calculated rate of diffusion.

Direct evidence for the break junction mechanism comes from atomic force microscopy (AFM) observations of individual Pd mesowires. Four AFM images of a Pd mesowire on a graphite surface (Fig. 6) track the structure of this mesowire in air (Fig. 6, A and C) and in pure H_2 (Fig. 6, B and D). The gap present in the Pd mesowire shown in Fig. 6A alternatively closes and reopens as the ambient gas is changed from air to hydrogen and back to air (10). After several exposures to H_2 , SEM images of mesowires (Fig. 1B) reveal the presence of 2 to 10 of these gaps for every 10 μm of wire length. A more detailed examination of the AFM data reveals that multiple grains slide in a concerted fashion to effect the opening and closing of these nanoscopic gaps. For the mesowire shown in Fig. 6, for example, the three grains to the left of the break junction move to the right by ≈ 50 nm to close the gap. The two grains to the right of the gap remain stationary ("pinned"). A second ensemble of at least four grains also moves to the right by 30 to 50 nm.

The motion of mesowire segments seen in Fig. 6 is the direct result of the swelling of individual Pd grains in the presence of H_2 . X-ray crystallographic data for the Pd hydride system (5) indicates that the lattice constant of Pd is 3.889 Å, whereas that for β -phase $PdH_{0.7}$, which is the thermodynamically stable form of Pd in equilibrium with 1.0 atm H_2 at 25°C, is 4.025 Å—an increase of 3.5%. For "pinned" grains which have an orientation on the surface that remains unchanged during switching, AFM images revealed a height increase of 2 to 3% in the presence of H_2 (Fig. 6E). Grains involved in sliding showed apparent height increases that ranged from 4 to 15%. These results may indicate a propensity of some Pd grains to be squeezed slightly up and out of the plane of the surface in the presence of H_2 .

The reversible and reproducible break junction dynamics we describe for electrodeposited Pd mesowires provides a new mechanism by which mesowires can operate as chemical sen-

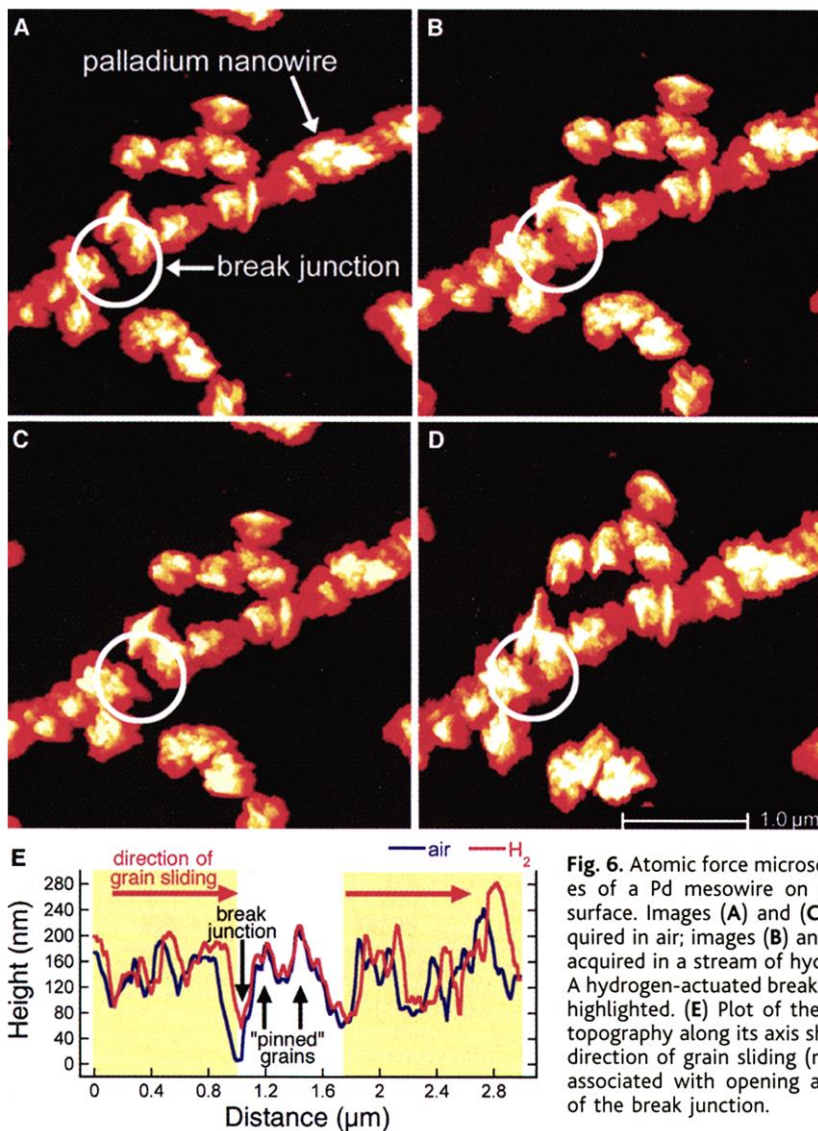


Fig. 6. Atomic force microscope images of a Pd mesowire on a graphite surface. Images (A) and (C) were acquired in air; images (B) and (D) were acquired in a stream of hydrogen gas. A hydrogen-actuated break junction is highlighted. (E) Plot of the mesowire topography along its axis showing the direction of grain sliding (red arrows) associated with opening and closing of the break junction.

sors. The performance of the mesowire array-based sensors documented here challenges existing H_2 sensing technologies. In particular, mesowire array-based H_2 sensors possess four attributes: (i) fast response; (ii) room-temperature operation; (iii) diminutive power requirements of less than 100 nW; and (iv) resistance to poisoning by reactive gases, including O_2 , CO, and CH_4 .

References and Notes

1. C. Z. Li, H. X. He, A. Bogozi, J. S. Bunch, N. J. Tao, *Appl. Phys. Lett.* **76**, 1333 (2000); C. Z. Li, H. Sha, N. J. Tao, *Phys. Rev. B* **58**, 6775 (1998); A. Bogozi et al., *J. Am. Chem. Soc.* **123**, 4585 (2001).

2. P. G. Collins, K. Bradley, M. Ishigami, A. Zettl, *Science* **287**, 1801 (2000).
 3. A. Zahab, L. Spina, P. Poncharal, C. Marliere, *Phys. Rev. B* **62**, 10000 (2000).
 4. J. Kong, H. J. Dai, *J. Phys. Chem. B* **105**, 2890 (2001); J. Kong et al., *Science* **287**, 622 (2000).
 5. Mesoscopic structures are characterized by a length scale ranging from tens of nanometers to micrometers.
 6. F. A. Lewis, *The Palladium Hydrogen System* (Academic Press, New York, 1967).
 7. M. P. Zach, K. Ng, R. M. Penner, *Science* **290**, 2120 (2000).
 8. Details of the deposition conditions and electron diffraction characterization are available on Science Online at www.sciencemag.org/cgi/content/full/293/5538/2227/DC1
 9. During hydrogen absorption into the nanowire, the diffusion coefficient will increase from a value char-

acteristic of the α phase ($D_\alpha = 1.6 \times 10^{-7} \text{ cm}^2 \text{ s}^{-1}$) to the β -phase value ($D_\beta = 5 \times 10^{-6} \text{ cm}^2 \text{ s}^{-1}$) (6).
 10. AFM measurements of palladium nanowires in functioning sensors have also been carried out. Reversible gap opening and closing is also observed in these nanowires, but the nanowire diameter can not be accurately measured because these wires are embedded in the cyanoacrylate film.
 11. This work was funded by the NSF (grant CHE-0111557) and the Petroleum Research Fund of the American Chemical Society (grant 33751-AC5). R.M.P. acknowledges the financial support of the A. P. Sloan Foundation Fellowship and the Camille and Henry Dreyfus Foundation. F.F. acknowledges funding through NATO. Finally, donations of graphite by A. Moore of Advanced Ceramics are gratefully acknowledged.

6 June 2001; accepted 7 August 2001

Changes in Seismic Anisotropy After Volcanic Eruptions: Evidence from Mount Ruapehu

Vicki Miller* and Martha Savage†

The eruptions of andesite volcanoes are explosively catastrophic and notoriously difficult to predict. Yet changes in shear waveforms observed after an eruption of Mount Ruapehu, New Zealand, suggest that forces generated by such volcanoes are powerful and dynamic enough to locally overprint the regional stress regime, which suggests a new method of monitoring volcanoes for future eruptions. These results show a change in shear-wave polarization with time and are interpreted as being due to a localized stress regime caused by the volcano, with a release in pressure after the eruption.

two separate deployments of broadband seismometers; the first during 1994 and the second in 1998 (14). The most recent large volcanic eruptions at Mount Ruapehu occurred in 1988 and 1995/96 (15). Local earthquakes within the shear-wave window (16, 17) were analyzed. For each deployment, there are two data sets. The first contains earthquakes with a local magnitude (M_L) ≥ 3 , with hypocenters deeper than 50 km. The second consists of events with depths shallower than 30 km and includes lower magnitudes (M_L 0.4 to 4.1). All seismograms were analyzed to determine the shear-wave splitting parameters ϕ and δt (18–21) [see (22) for examples of waveforms].

The average ϕ for both the shallow data sets (Fig. 1, A and B) is NW-SE. The 1994 average is $(\phi, \delta t) = (313^\circ \pm 7^\circ, 0.10 \pm 0.01 \text{ s})$. The 1998 average is $(293^\circ \pm 12^\circ, 0.10 \pm 0.01 \text{ s})$. There is a greater variation in individual azimuths for 1998 [from 19° variation in 1994 to 47° in 1998 (21)].

The 1994 deep data set (Fig. 1C) average ϕ is NW-SE ($324^\circ \pm 6^\circ, 0.17 \pm 0.03 \text{ s}$), similar to the shallow results. The deep 1998 data set (Fig. 1D) however, has an average ϕ of ENE-WSW ($250^\circ \pm 14^\circ, 0.11 \pm 0.01 \text{ s}$); this is almost perpendicular to both the deep and shallow 1994 data sets.

The large scatter in most of the data sets may be caused by the irregular surface topography in the region. The NW-SE ϕ of the shallow data sets and the 1994 deep data sets is almost perpendicular to the maximum compressive stress axis of the surrounding Taupo Volcanic Zone (TVZ) and the alignment of the most recently active [$<10,000$ years ago] (23) vents (NNE-SSW). Two possible interpretations for the changes in ϕ are (i) changes from high to lower pore pressures or (ii) changes in crack orientations.

We interpret ϕ in 1994 as resulting from localized stress caused by the volcano, with a pressure source from a NNE-SSW-trending tabular (24) magma body, such as that indicated by regions of anomalously high S-wave attenuation or “shadowing” (25) (Fig. 2); the geometry of the magma body is induced by

The prediction of volcanic eruptions is one of the primary goals of hazards research. Changes in stress indicators would be particularly useful in understanding the buildup of stress and strain before an eruption. One suggested method of monitoring stress is to observe changes in shear-wave splitting. Shear-wave splitting occurs when elastic waves enter an anisotropic medium. The energy is split into two components, in which the component polarized in one direction travels faster than its orthogonal counterpart. Shear-wave splitting in the upper 10 to 15 km of the crust may result from fluid-filled cracks, microcracks, preferentially oriented pore space, or a combination of these factors (1, 2). Differential stress preferentially closes cracks that are aligned perpendicular to the maximum principal stress. The cracks that remain open are thus aligned perpendicular to the minimum horizontal compressional stress axis. The initial polarization (the “fast direction” or ϕ) of shear-wave splitting in cracked media is parallel to the cracks and therefore to the maximum compressive stress.

The time delay (δt) between the arrival of the two components depends on the path length and on the amount of anisotropy in the particular ray path direction through the material. Initial polarizations are a more robust feature than δt , which typically shows considerable scatter (3–6). Because of these difficulties, controversy continues as to whether changes reported in δt are caused by changes in the stress regime due to earthquakes and volcanic activity or are due simply to path differences (3, 4, 7, 8). Slight changes of 7° to 10° in ϕ during hydraulic pumping in a hot, dry, rock geothermal reservoir were suggested (9), whereas temporal variations in ϕ related to tectonic and/or volcanic activity have not been reported.

Work on volcanic systems and rift zones has yielded ϕ of shear-wave splitting generally parallel to the maximum principal stress [for example, the Michoacan-Guanajuato volcanic field (10), Mexico; the Kilauea East Rift Zone, Hawaii; and the Phlegrean Fields (11), Italy]. However, studies in the Long Valley Caldera, California (12), and on the volcano Mount Vesuvius, Italy (13), yielded ϕ aligned with regional faulting rather than the local stress direction.

On the volcano Mount Ruapehu, New Zealand, ϕ and δt were determined with data from

Institute of Geophysics, Victoria University of Wellington, Wellington, New Zealand.

*Present address: Upper Hutt City Council, Private Bag 907, Upper Hutt, New Zealand.

†To whom correspondence should be addressed. E-mail: Martha.Savage@vuw.ac.nz